A&A, 707, L14 (2026)
https://doi.org/10.1051/0004-6361/202658976

Astronomy & Astrophysics

LETTER TO THE EDITOR

First Sardinia Radio Telescope detection of the Sunyaev-Zel'dovich effect at 18.6 GHz

S. Cocchi[1,2,3,⋆], F. Loi[2], M. Murgia[2], P. Marchegiani[2], V. Vacca[2], F. Govoni[2], F. Gandossi[1,2,3], and G. Rodighiero[4]

[1] Dipartimento di Fisica e Astronomia, Università di Bologna, Via P. Gobetti 93/2, 40129 Bologna, Italy
[2] INAF-Osservatorio Astronomico di Cagliari, Via della Scienza 5, I-09047 Selargius, (CA), Italy
[3] INAF, Istituto di Radio Astronomia, Via Gobetti 101, 40129 Bologna, Italy
[4] Dipartimento di Fisica e Astronomia, Università degli Studi di Padova, Vicolo dell'Osservatorio 3, I-35122 Padova, Italy

Received 15 January 2026 / Accepted 21 February 2026

ABSTRACT

Galaxy clusters imprint a distinctive signature on the cosmic microwave background through the thermal Sunyaev–Zel'dovich (SZ) effect, which enables to study the intracluster plasma distribution and makes them powerful cosmological probes. We present the first Sardinia Radio Telescope (SRT) detection of the SZ effect in the galaxy cluster MACS J1752+4440 at 18.6 GHz, with a resolution of 0.9′. We detected a decrement in brightness toward the cluster centre, which we attributed to the thermal SZ effect. We modelled the signal using a spherically symmetric β model for the electron density distribution and we employed a Bayesian retrieval to estimate the core radius, central electron density, and β parameter of the cluster. We found values consistent with expectations for a galaxy cluster of the mass of MACS J1752+4440: a core radius of (160 ± 30) kpc, a central electron density of $(2.5^{+0.7}_{-0.5} \cdot 10^{-3})$ cm^{-3}, and $\beta = 0.6 \pm 0.1$. The mean Compton-y parameter within a radius of 3.5′ is $(2.6 \pm 0.3) \cdot 10^{-5}$, higher than the value reported by Planck, which is coherent considering the different resolution of the instruments and the modelling adopted. This work demonstrates the potential of the SRT to detect the onset of the SZ decrement at low frequencies, providing higher angular resolution than current all-sky surveys and enabling an improved reconstruction of the SZ decrement profile and the plasma distribution in the intracluster medium.

Key words. galaxies: clusters: general – cosmology: observations – radio continuum: general

1. Introduction

Clusters of galaxies, as the largest gravitationally bound systems in the Universe, are investigated at all frequencies, from the radio to the optical to the X-ray. In particular, at millimeter wavelengths, they imprint signatures on the Cosmic Microwave Background (CMB) through the Sunyaev–Zel'dovich (SZ) effect (Sunyaev & Zeldovich 1972). The SZ effect results from the inverse Compton scattering of CMB photons by thermal electrons in the intracluster medium (ICM). By shifting photons to higher frequencies, this process generates a characteristic spectral distortion: a decrement in CMB intensity at low frequencies that transitions to an increment above ∼220 GHz. This effect can be separated into two components: the kinetic SZ (kSZ) effect (e.g., Sunyaev & Zeldovich 1980), due to the cluster's line-of-sight motion, and the thermal SZ (tSZ) effect, which traces the thermal pressure and dynamics of the hot ICM. The tSZ effect has been widely used to detect and characterise galaxy clusters, with large surveys yielding catalogues of $\sim 10^2$–10^3 systems. It offers a nearly mass-limited census of the cluster population at high redshift (where the abundance is sensitive to cosmological parameters), while avoiding X-ray selection biases that favour nearby, dynamically relaxed systems (e.g. Planck Collaboration XXVII 2016). The Planck Collaboration selected through the SZ effect over 1600 systems between 100 and 857 GHz (Planck Collaboration I 2020). The South Pole Telescope (SPT; Reichardt et al. 2013) surveyed a catalogue of over 1000 SZ-selected clusters (Bleem et al. 2020), while the Atacama Cosmology Telescope (ACT) survey reported over 10000 SZ-detected clusters at 90−220 GHz (Aguena et al. 2026). However, these surveys have relatively poor angular resolutions: 5′ for Planck, and about 1′ for SPT and ACT. A higher resolution imaging of the tSZ effect was obtained using, for instance, MUSTANG-2, a 223-feedhorn bolometer camera mounted on the 100-meter Green Bank Telescope (GBT) (Dicker et al. 2014). Operating at 90 GHz with ∼9″ resolution and a 4.2′ field of view, MUSTANG-2 resolves ICM substructures such as shocks and pressure discontinuities that are inaccessible to survey-class experiments (Romero et al. 2020). NIKA2 (Adam et al. 2018) provides 17.6″ resolution at 150 GHz, enabling the detection of low-mass clusters out to intermediate and high redshifts (Chérouvrier et al. 2025). New Kinetic Inductance Detector (KID) based bolometric cameras are further advancing high-resolution millimetre observations: MISTRAL, installed at the 64-m Sardinia Radio Telescope (SRT), operates at 90 GHz with a 4′ field of view and ∼12″ resolution, optimised for SZ and diffuse emission studies (Battistelli et al., in prep.; Murgia et al., in prep.); TolTEC on the 50-meter Large Millimeter Telescope (LMT) provides simultaneous, polarisation-sensitive imaging across 143, 214, and 273 GHz, enabling precise separation of the thermal SZ effect from dusty star-forming galaxies with resolution of 5″ (Bryan et al. 2018).

In this Letter, we report the first SRT (Bolli et al. 2015; Prandoni et al. 2017) detection of the SZ effect in a galaxy cluster at 18.6 GHz. The result presented here is a serendipitous

⋆ Corresponding author: silvia.cocchi@inaf.it

discovery in the context of a project aimed at investigating the properties of the double radio relic system in the galaxy cluster MACS J1725+4440 ($z = 0.366$, Edge et al. 2003). At these frequencies, diffuse radio sources such as relics are affected by contamination from this effect, so properly characterizing it is essential for obtaining accurate flux density measurements (Basu et al. 2016). MACS J1752+4440, centred at $\mathrm{RA_{J2000}} = 17^{\mathrm{h}}52^{\mathrm{m}}01.5^{\mathrm{s}}$ and $\mathrm{Dec_{J2000}} = +44°40'46''$ according to the ROSAT All Sky Survey (RASS; Voges et al. 1999), was discovered in the Massive Cluster Survey (Ebeling et al. 2001) and later identified as a radio bright cluster by Edge et al. (2003) through a joint analysis of the Westerbork (WSRT) Northern Sky Survey (Rengelink et al. 1997) and RASS Bright Source Catalog. Radio studies with the WSRT (van Weeren et al. 2012) and Giant Microwave Radio Telescope (GMRT) (Bonafede et al. 2012) revealed it to be a merging double relic cluster. The SZ-derived mass[1] reported by the Planck Collaboration XXVII (2016) $M_{500} = (6.7^{+0.4}_{-0.5}) \cdot 10^{14}\, M_{\odot}$ is consistent within 1σ with the total mass $M_{500} = (1.47^{+0.33}_{-0.38}) \cdot 10^{15}\, M_{\odot}$ derived from Subaru and XMM–Newton data, according to Finner et al. (2021).

The contents of this Letter are organised as follows. Sect. 2 reports the details of observations and data reduction pipeline. The total intensity results are presented in Sect. 3, highlighting the detection of the SZ decrement in the centre of the cluster. Our modelling process is presented in Sect. 4. Finally, the summary and conclusions are given in Sect. 5. Throughout this work we assume a flat ΛCDM cosmology with $H_0 = 70\,\mathrm{km\,s^{-1}\,Mpc^{-1}}$, $\Omega_{\mathrm{m}} = 0.3$, and $\Omega_{\Lambda} = 0.7$. At the redshift of MACS J1752+4440, $1'$ corresponds to ∼305 kpc.

2. Observations and data reduction

With the SRT, we observed an area of $10' \times 10'$ centred on MACS J1752.0+4440 centre with the seven-feed K-band receiver, with a bandwidth of 1200 MHz centred at 18.6 GHz (project code 18–23, P.I. Francesca Loi). The observations were carried out between November 2024 and January 2025, with the SARDARA backend (SArdinia Roach2-based Digital Architecture for Radio Astronomy, Melis et al. 2018). We performed on-the-fly (OTF; Mangum et al. 2007) mapping in the equatorial frame, alternating the RA and Dec directions. The use of orthogonal maps enables the identification and mitigation of scanning correlated noise through de-striping techniques (as described in Appendix A.1 of Murgia et al. 2016). The telescope scanning speed was set to $2'$/s and the scans were separated by $0.25'$ to properly sample the SRT beam with at least 4 pixels. Data were taken on 15 different days, with observations lasting 5.5 hours each (80% of them on-source) for a total of 82.5 hours.

The data reduction was carried out with the proprietary Single-dish Spectral-polarimetry Software (SCUBE; Murgia et al. 2016), following a procedure similar to those previously described by Loi et al. (2020) and Bianchi et al. (2022). Spectral channels affected by backend issues were first flagged, followed by an automatic removal of outliers and radio frequency interferences (RFI). Observations of the cold sky with and without an injected signal were used to correct gain and delay differences between right- and left-hand polarisations. Atmospheric contributions were removed using skydip scans to estimate atmospheric opacity and system temperature (Buffa et al. 2016). Since the data were collected in 15 separate observing sessions, any residual atmospheric noise is expected to behave randomly across the field of view.

[1] M_{500} is defined as the mass enclosed in R_{500}, where the density is 500 times the critical density of the Universe.

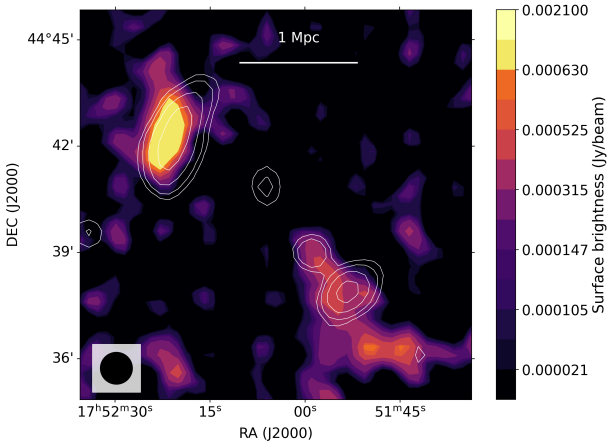

Fig. 1. SRT total intensity image at 18.6 GHz with beam of $0.9'$, pixel size of $15''$. Contours at 2, 3, 5, 10, and $20\sigma_{\mathrm{NVSS}}$ from the NVSS image (Condon et al. 1998) at 1.4 GHz, with $\sigma_{\mathrm{NVSS}} = 0.4$ mJy/beam.

Baselines were subtracted using the first and last 10% of each subscan. Bandpass calibration was performed using 3C286 to correct the frequency-dependent response of the seven K-band feeds (Orfei et al. 2010). After applying all the previous terms, the calibrators data were then gridded with a scale of $15''$ per pixel. Then a flux density scale calibration was performed with 3C286. For each of the seven feeds and for both left- and right-hand circular polarisations (LCP and RCP), a 2D Gaussian was fitted to the calibrator maps using a combination of random search and gradient descent. The conversion from counts to Jansky was applied using the flux-density model from Perley & Butler (2013). The flux calibration was applied to 3C295, which was used to assess the calibration accuracy by comparing the results with the theoretical values at 17.975 GHz. A 2D Gaussian was fitted to each calibrated image and the relative errors, computed as the difference between measured and expected peak flux, then normalised by the latter, were evaluated across all feeds, polarisations, and scan pairs. The distribution of these errors was used to identify new outliers arising after flux calibration, likely due to residual RFI, and an additional manual flagging step was applied, ensuring that the remaining calibration error was kept below 10%. After applying the calibration solutions to the galaxy cluster data, a baseline subtraction was applied to individual subscans using second-order polynomials, excluding masked regions to avoid bright-source contamination; the mask was constructed from the $3\sigma_{\mathrm{NVSS}}$ contours at 1.4 GHz (see Figure 1). Masking and polynomial subtraction prevent a potential negative bias at the map centre. Baseline fitting was iteratively refined with 5σ clipping. Gridded maps were created with a resolution of 128×128 pixels and a pixel scale of $15''$. We combined the calibrated LCP and RCP data to form separate Stokes I images for the RA and Dec scans using weighted stacking (Murgia & Fatigoni 2024). The two final RA and Dec maps were then merged using a wavelet-based method (Murgia et al. 2016) to enhance the signal-to-noise ratio (S/N) and destripe the residual scanning noise.

3. Total intensity results and decrement detection

Figure 1 shows the resulting 18.6 GHz SRT image obtained by averaging the data between 18 GHz and 19.2 GHz. The noise is $\sigma = 0.2$ mJy/beam, the beam size is $0.9'$.

The image captures the emission from the northern relic at 3σ; however, it cannot separate, at 2σ, the emission of the

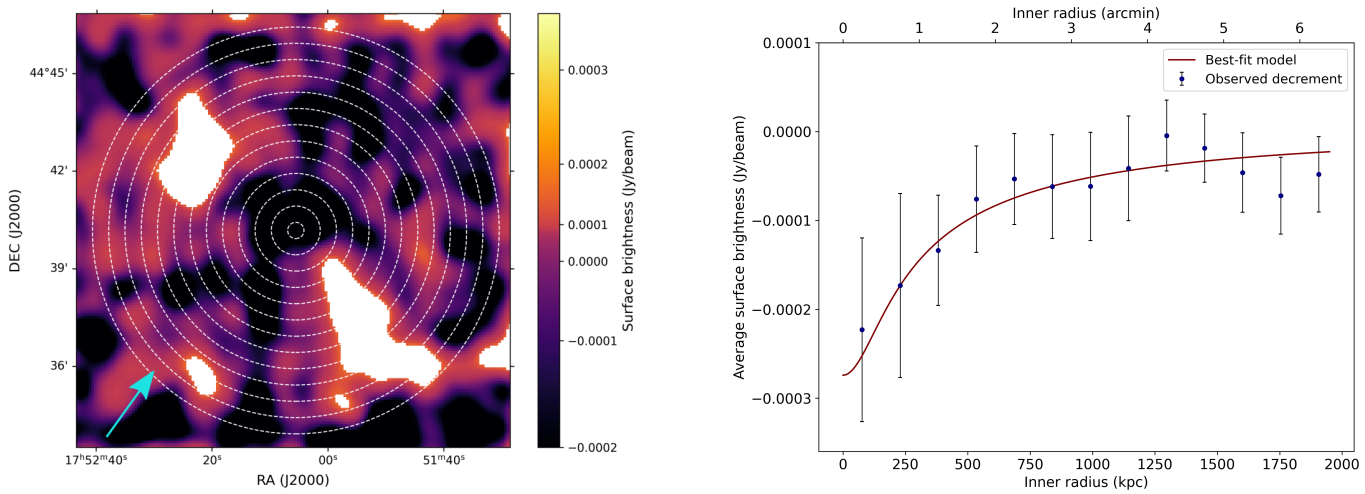

Fig. 2. *Left*: Map of the observed surface brightness decrement in the cluster centre from SRT data at 18.6 GHz. The profile reported on the right was obtained by blanking the radio sources and tracing annuli around the centre of the cluster, at intervals of a half-beam radius from one another. The blue arrow marks a localised surface-brightness excess in the south-eastern region. *Right*: Observed average surface brightness on annuli around the centre of the cluster, in blue. The continuous line shows the fit of the SZ decrement referred to the models from Eqs. (2) and (4).

southern radio relic and of the source just northeast of it, which has been assumed to be a radio galaxy in previous works (see Bonafede et al. 2012; van Weeren et al. 2012). The SRT detects emission from the northern relic centred in a different region with respect to the NVSS, likely because at 18.6 GHz, the SRT is more sensitive to the outer edge of the relic, closest to the shock front where particle acceleration occurs and the spectrum is relatively flat. Toward the cluster centre, radiative losses suppress the population of electrons emitting at such high frequencies, whereas electrons emitting at 1.4 GHz are still present. The left panel of Figure 2 allows us to visualise an evident surface brightness decrement at the cluster centre, which we attribute to the tSZ effect. This image was produced by applying a Gaussian smoothing ($\sigma_{\rm smooth} = 2$ pixels) to the data, after masking out the emission from the radio sources from SRT data at 1σ, and subsequently upscaling the image by a factor of three using cubic interpolation to enhance visualisation. The radial surface-brightness profile, measured in azimuthal segments, is largely circularly symmetric, except for a bump between ∼1200 and 1600 kpc (Figure 2), corresponding to a localised excess in the southeastern region of the cluster (cyan arrow), which should be taken into account for future observations of the cluster. The profile of the detected intensity decrement due to the SZ effect is reported on the right panel of Figure 2. Each point shows the mean surface brightness in the concentric annuli of Figure 2, with uncertainties given by the standard deviation divided by the square root of the number of beams in each annulus. We estimated the S/N of the SZ decrement by defining the signal, ΔI_i, as the difference between every decrement measurement and the outer plateau reached beyond ∼1200 kpc, of $(4.0 \pm 0.9) \times 10^{-5}$ Jy beam^{-1}, then computing the noise as the quadrature sum of the uncertainties of the annuli used in the measurement,

$$S/N = \frac{\sum \Delta I_i}{\sqrt{\sum \sigma_i^2}}. \tag{1}$$

Thus, we obtained a S/N of 3. The cluster centre was defined by the peak SZ decrement. While SZ and X-ray centres can differ in merging systems, our SZ centre ($\mathrm{RA_{J2000}} = 17^{\rm h}52^{\rm m}0.5^{\rm s}$, $\mathrm{Dec_{J2000}} = +44°40'46''$) coincides, at our pixel scale, with the RASS position (Table 1 in Bonafede et al. 2012).

4. Decrement modelling

The observed decrement was compared with a model prediction. At cm wavelengths, in the Rayleigh-Jeans approximation, Basu et al. (2016) derived the theoretical decrement, $\Delta I_{\rm SZ}$,

$$\left(\frac{\Delta I_{\rm SZ}}{\rm mJy/beam}\right) = \frac{1}{340}\left(\frac{\nu}{\rm GHz}\right)^2\left(\frac{\Delta T_{\rm RJ}}{\rm mK}\right)\left(\frac{\Omega_{\rm beam}}{\rm arcmin^2}\right), \tag{2}$$

where ν is the observing frequency in GHz, $\Omega_{\rm beam}$ is the beam solid angle in square arcminutes, and $\Delta T_{\rm RJ} = -2 \cdot y \cdot T_{\rm CMB}$ with $T_{\rm CMB}$ the CMB temperature. The Compton y-parameter is defined as (e.g. Birkinshaw 1999):

$$y = \int n_e(r)\sigma_{\rm T}\frac{k_{\rm B}T_e(r)}{m_e c^2}\,{\rm d}l, \tag{3}$$

where n_e is the electron density, $\sigma_{\rm T}$ the Thomson scattering cross section, T_e the ICM temperature, m_e the electron mass, and c the speed of light. We integrated along the line of sight, l. The electron density has been assumed to follow a simple spherically symmetric β-model, described by

$$n_e(r) = n_0\left(1 + \frac{r^2}{r_c^2}\right)^{-3\beta/2}, \tag{4}$$

where n_0 is the central electron density of the cluster and r_c is the core radius.

A best-fit set of parameters n_0, r_c, and β was obtained using a Markov chain Monte Carlo (MCMC) approach with the *emcee* sampler (Foreman-Mackey et al. 2013) and uniform priors, assuming an isothermal model for the cluster with $k_{\rm B}T_e = 5.9$ keV (Finner et al. 2021). The results are listed in Table 1, with posterior distributions shown in the corner plot in Figure A.1. The corner plot highlights the correlation between the β parameter and the core radius, as we would expect from the model adopted. Nevertheless, the derived parameters are consistent with expectations for a cluster of the mass of MACS J1752+4440 (for studies on other clusters, see e.g. Pointecouteau et al. 2002; Bonamente et al. 2006), demonstrating that even this simplified model can effectively offer a starting point in the characterisation of galaxy clusters.

Table 1. Retrieved β-model parameters from MCMC sampling.

Parameter	Median	$-\sigma$	σ
r_c [kpc]	160	−30	+30
$\log n_0$ [cm^{-3}]	−2.6	−0.1	+0.1
β	0.6	−0.1	+0.1

Notes. Quoted values are medians with 16th and 84th percentile uncertainties.

5. Discussion and conclusions

We report the first SRT detection of the tSZ effect at 18.6 GHz in MACS J1752+4440, revealing a central surface-brightness decrement. The signal was modelled using the profile of Basu et al. (2016), adopting a spherical β model for the electron density. An MCMC analysis was used to constrain the central density, core radius, and β value. Given the merging nature of MACS J1752, these parameters should be considered as effective quantities, describing the average SZ signal, rather than the true 3D ICM structure; nevertheless, they are physically consistent with expectations for a cluster of this mass. To our knowledge, no estimates of these parameters have been published from X-ray data to date. By inverting Eq. (2) and averaging within a 3.5′ radius (half the Planck beam), we obtained $y^{0.9'}_{\rm SRT} = (2.3 \pm 0.3) \cdot 10^{-5}$. Convolving the SRT map with the 7′ Planck beam yields $y^{7'}_{\rm SRT} = (1.8 \pm 0.3) \cdot 10^{-5}$, higher than the Planck MILCA value of $y_{\rm Planck} = (4 \pm 1) \cdot 10^{-6}$ (Planck Collaboration XXVII 2016)[2]. This discrepancy is largely explained by angular-resolution effects. Planck's 7′ beam smooths the signal on cluster scales, leading to an underestimation of Compton-y by factors of ∼3 (e.g. Aghanim et al. 2019). The higher resolution of the SRT also enables subtraction of contaminating radio sources: a typical ∼1 mJy source contributes $\Delta y \sim 10^{-6}$ (Eq. (2), Planck beam at ∼100 GHz), comparable to Planck sensitivity, but negligible after a correction on the SRT map. Our simplified spherical β model introduces additional effects. Neglecting cluster geometry or any departures from isothermality can bias SZ- and X-ray-derived parameters by up to ∼30% (Puy et al. 2000). Assuming an infinite line-of-sight depth further overestimates $y^{7'}_{\rm SRT}$ by projecting more gas than is physically present. Departures from spherical symmetry can modify both the amplitude and the shape of the inferred Compton-y profile: an elongation along the line of sight enhances the SZ signal, while asymmetries in the plane of the sky are smoothed by azimuthal averaging, producing a flatter effective profile. Such considerations underscore the need for cluster-specific modelling, while supporting the robustness of the SRT detection given the model simplifications and the different angular resolution of Planck. Previous SZ measurements at 15−20 GHz have mainly relied on interferometric observations (e.g. Massardi et al. 2010; AMI Consortium 2011), which are intrinsically limited in their sensitivity to diffuse emission on arcminute scales due to missing short baselines. The SRT K-band observations probe a complementary regime, providing sensitivity to extended SZ signals on arcminute scales at low frequencies and enabling the joint characterisation of thermal and non-thermal ICM components on cluster scales, which is a frequency-angular-scale parameter space that is not fully covered by current higher resolution interferometric or mm-wave facilities. At 18.6 GHz, these observations only probe the low-frequency tail of the SZ spectral distortion, which reaches its minimum near 150 GHz and, therefore, they are not intended as primary means for SZ studies. However, they demonstrate the high sensitivity of the SRT and its capacity to detect and characterise SZ signals at low frequencies at a higher resolution than Planck. Moreover, the detection of the SZ decrement during observations aimed at studying diffuse cluster emission represents an added value of such datasets: a preliminary estimate of the Compton-y parameter can inform the selection of promising targets for follow-up observations; for instance, at 90 GHz with the MISTRAL receiver at the SRT.

[2] Data taken from MILCA (Hurier et al. 2013) 7′ map, https://szdb.osups.universite-paris-saclay.fr/ymap.html

Acknowledgements. The Enhancement of the Sardinia Radio Telescope (SRT) for the study of the Universe at high radio frequencies is financially supported by the National Operative Program (Programma Operativo Nazionale – PON) of the Italian Ministry of University and Research "Research and Innovation 2014-2020", Notice D.D. 424 of 28/02/2018 for the granting of funding aimed at strengthening research infrastructures, in implementation of the Action II.1 – Project Proposals PIR01 00010 and CIR01 00010. This work was carried out thanks to the funding of the Regione Autonoma della Sardegna, ai sensi della Legge Regionale 7 agosto 2007, n.7 Promozione della Ricerca Scientifica e dell'Innovazione Tecnologica in Sardegna. SC acknowledges support from the ERC CoG ***B***ELOVED, GA N.101169773. We thank the referee for comments and suggestions.

References

Adam, R., Adane, A., Ade, P. A. R., et al. 2018, A&A, 609, A115
Aghanim, N., Douspis, M., Hurier, G., et al. 2019, A&A, 632, A47
Aguena, M., Aiola, S., Allam, S., et al. 2026, Open J. Astrophys., 9, 55863
AMI Consortium (Rodríguez-Gonzálvez, C., et al.) 2011, MNRAS, 414, 3751
Basu, K., Vazza, F., Erler, J., & Sommer, M. 2016, A&A, 591, A142
Bianchi, S., Murgia, M., Melis, A., et al. 2022, A&A, 658, L8
Birkinshaw, M. 1999, Phys. Rep., 310, 97
Bleem, L. E., Bocquet, S., Stalder, B., et al. 2020, ApJS, 247, 25
Bolli, P., Orlati, A., Stringhetti, L., et al. 2015, J. Astron. Instrum., 4, 1550008
Bonafede, A., Brüggen, M., van Weeren, R., et al. 2012, MNRAS, 426, 40
Bonamente, M., Joy, M. K., LaRoque, S. J., et al. 2006, ApJ, 647, 25
Bryan, S., Austermann, J., Ferrusca, D., et al. 2018, SPIE Conf. Ser., 10708, 107080J
Buffa, F., Serra, G., Bolli, P., et al. 2016, K-band System Temperature Forecast for the Sardinia Radio Telescope, 54
Chérouvrier, D., Macías-Pérez, J. F., Désert, F. X., et al. 2025, A&A, 700, A30
Condon, J. J., Cotton, W. D., Greisen, E. W., et al. 1998, AJ, 115, 1693
Dicker, S. R., Ade, P. A. R., Aguirre, J., et al. 2014, J. Low Temp. Phys., 176, 808
Ebeling, H., Edge, A. C., & Henry, J. P. 2001, ApJ, 553, 668
Edge, A. C., Ebeling, H., Bremer, M., et al. 2003, MNRAS, 339, 913
Finner, K., HyeongHan, K., Jee, M. J., et al. 2021, ApJ, 918, 72
Foreman-Mackey, D., Hogg, D. W., Lang, D., & Goodman, J. 2013, PASP, 125, 306
Hurier, G., Macías-Pérez, J. F., & Hildebrandt, S. 2013, A&A, 558, A118
Loi, F., Murgia, M., Vacca, V., et al. 2020, MNRAS, 498, 1628
Mangum, J. G., Emerson, D. T., & Greisen, E. W. 2007, A&A, 474, 679
Massardi, M., Ekers, R. D., Ellis, S. C., & Maughan, B. 2010, ApJ, 718, L23
Melis, A., Concu, R., Trois, A., et al. 2018, J. Astron. Instrum., 7, 1850004
Murgia, G., & Fatigoni, S. 2024, ApJS, 272, 10
Murgia, M., Govoni, F., Carretti, E., et al. 2016, MNRAS, 461, 3516
Orfei, A., Carbonaro, L., Cattani, A., et al. 2010, IEEE Antennas Propag. Mag., 52, 62
Perley, R. A., & Butler, B. J. 2013, ApJS, 204, 19
Planck Collaboration XXVII. 2016, A&A, 594, A27
Planck Collaboration I. 2020, A&A, 641, A1
Pointecouteau, E., Hattori, M., Neumann, D., et al. 2002, A&A, 387, 56
Prandoni, I., Murgia, M., Tarchi, A., et al. 2017, A&A, 608, A40
Puy, D., Grenacher, L., Jetzer, P., & Signore, M. 2000, A&A, 363, 415
Reichardt, C. L., Stalder, B., Bleem, L. E., et al. 2013, ApJ, 763, 127
Rengelink, R. B., Tang, Y., de Bruyn, A. G., et al. 1997, A&AS, 124, 259
Romero, C. E., Sievers, J., Ghirardini, V., et al. 2020, ApJ, 891, 90
Sunyaev, R. A., & Zeldovich, Y. B. 1972, Comments Astrophys. Space Phys., 4, 173
Sunyaev, R. A., & Zeldovich, Y. B. 1980, MNRAS, 190, 413
van Weeren, R. J., Bonafede, A., Ebeling, H., et al. 2012, MNRAS, 425, L36
Voges, W., Aschenbach, B., Boller, T., et al. 1999, A&A, 349, 389

Appendix A: Parameter retrieval: Corner plot

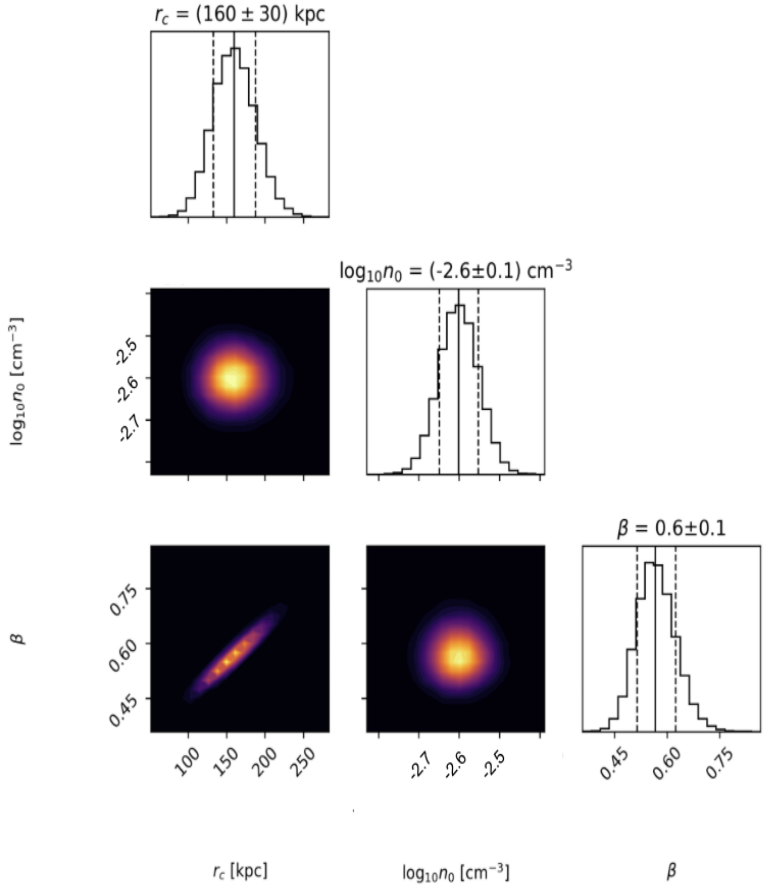

Fig. A.1. Retrieval of parameters for the density profile using *emcee*. The continuous line represents the median of the distribution. The dashed lines show the 16th and 84th percentiles.